Sar-Gel Visualization of Inhaled Vapors in Human Nasal and Lung Casts

Jinxiang Xi[1,2*]

[1]*Department of Aerospace and Mechanical Engineering, California Baptist University, Riverside, CA, 92504, USA*

[2]*Department of Biomedical Engineering, California Baptist University, Riverside, CA, 92504, USA*

Abstract: An accurate knowledge of drug distribution in human airways after drug administration is critical in establishing dose-response correlations and optimizing the treatment outcomes. However, human airways are inaccessible to conventional instruments, making it challenging to visualize and quantify local deposition within. This paper presented a simple but effective method to characterize local depositions in the human respiratory tract. Sar-Gel was used to visualize the deposition pattern and a colorimetry approach was developed to quantify the deposition fractions. Two examples were given, one being the nasal delivery and the other being pulmonary delivery. Anatomically accurate image-based model geometries were used in both examples. Computational modeling and simulations were also employed to cross-validate the corresponding *in vitro* tests. Results vividly show the variation of aerosol deposition distributions in response to different inhaler devices and breathing conditions. An excellent match was obtained in the surface deposition between *in vitro* tests and numerical simulations. The empirical colorimetry method slightly underestimated the direct weighing method but agreed well in the deposition trend. The Sar-Gel visualization approach in sectional respiratory tract casts seems to be a simple and effective way to characterize local vapor deposition. Sar-Gel visualization and numerical simulations can be complementary to each other in assessing device performance and optimizing inhalation drug deliveries.

Keywords: Sar-Gel visualization, aerosol deposition distribution, nebulizer, nasal drug delivery, pulmonary delivery.

1. INTRODUCTION

An important factor in respiratory drug delivery is to know where the medications end up and how many agents get to the target. Both the total and the local depositions are critical to the clinical outcome of an inhalation therapy [1,2]. Therefore, it is cruical to quantify the aerosol deposition distribution in different airway regions.

The human respiratory tract is inaccessible to conventional visualization and quantification tools except for the radioactive imaging techniques. Such imaging techniques include gamma scintigraphy, Positron Emission Tomography (PET), and Single Photon Emission Computerized Tomography (SPECT). Two-dimensional or three-dimensional aerosol distributions can be obtained using these imaging techniques, which have proven invaluable in testing the performance of inhalation devices [3]. However, one major setback of the imaging techniques is the radioactive risk exposed to the subjects [4,5]. Other setbacks include cost, availability, and operational complexities [4,5]. Numerical modeling and simulations have also been extensively used in the inhalation device design and environmental health risk assessment [6,7]. Flow details can be easily captured using numerical simulations, which are often difficult to obtain in experiments. However, inhalation drug delivery is a process that can be complicated by a variety of factors, such as inhalation devices, breathing conditions, patient health status, and drug formulations. Many assumptions are needed to make the modeling practical. In this sense, many compounding factors are neglected, which may or may not significantly alter the aerosol behaviors. It is also noted that current *in vitro* tests in quantifying dosimetry often utilized casts that are not transparent, nor can be opened apart. Therefore, visualization of the deposition distributions inside the casts is not feasible. It is important to develop a technique that can visualize and quantify the aerosol deposition within human respiratory tract in a simple, reliable, and safe manner [8].

Dalby and collaborators [9-11] have used Sar-Gel (Sartomer, PA) to visualize qualitatively aerosol deposition distributions in transparent nasal casts. Sar-Gel is a chemical that changes into pink in contact with moisture and has been shown to be sensitive enough to a moisture mass as low as 0.5 μL [10,11]. In several recent studies, Xi *et al*. [12,13,5] used Sar-Gel to visualize the deposition distributions in sectional airway cast replicas using various types of nasal spray pumps and nebulizers_ENREF_32. A Sar-Gel deposition image shows different color levels depending on the

*Address correspondence to this author at the Department of Aerospace and Mechanical Engineering, Gordon and Jill Bourns College of Engineering, California Baptist University, 432 Magnolia Ave, Riverside, CA 92504;
Tel: (951) 552-8084; Fax: (951) 343-4972; E-mail: jxi@calbaptist.edu

E-ISSN: 2310-9394/17

deposited mass of the inhaled droplets. This colorimetry-mass correlation can be exploited to quantify the deposition and be used as an auxiliary method to the more complex and costly imaging approaches.

This paper reviews the recent attempts in our lab using Sar-Gel to visualize the vapor/droplets distributions in the nasal cavity and mouth-lung geometry models. Computational simulations of corresponding *in vitro* experiments have been conducted and the results have been compared to the experimental data. In the following text, experimental methods and materials will be described in section 2. The experimental results of vapor deposition in the nasal cavity and mouth-lung geometry will be presented in section 3. Potential implications of these results and significance of the Sar-Gel method will be discussed in section 4.

2. METHODS AND MATERIALS

2.1. *In Vitro* Experiment Design

To visualize the local deposition in the human respiratory tract, hollow cast replicas of anatomically accurate nasal and mouth-lung models were prepared in this study. Software Magics (Materialise, Ann Arbor, MI) was used to prepare the hollow airway replicas from the nasal airway and mouth-lung model geometries [13,5]. These hollow casts have a constant wall thickness of 4 mm [14]. The casts were divided into different sections to measure sub-regional deposition rates. Grooves were designed at the connecting ends to facilitate sealing and assembly between different parts [15,16]. The influence of drug release position, electric field, magnetic control, and pulsating flow were studied on the efficiency of olfactory delivery [17]. The hollow casts were manufactured with a Stratasys Objet30 Pro 3-D printer (Northville, MI). This printer has a high printing resolution of 16 μm. Polypropylene, a transparent material, was utilized to fabricate the hollow model that the deposition patterns can be viewed from the outside of the casts.

Nasal spray (Astelin) was used for nasal delivery (Figure **1b**). An electronic balance was used to measure the output per dosing as the mass difference before and after the spray release. Four types of nebulizers were considered: jet (Philips Respironics), PARI Sinus, Ultrasonic (Respironics), and vibrating mesh (Drive Voyager Pro) (Figure **1b**).

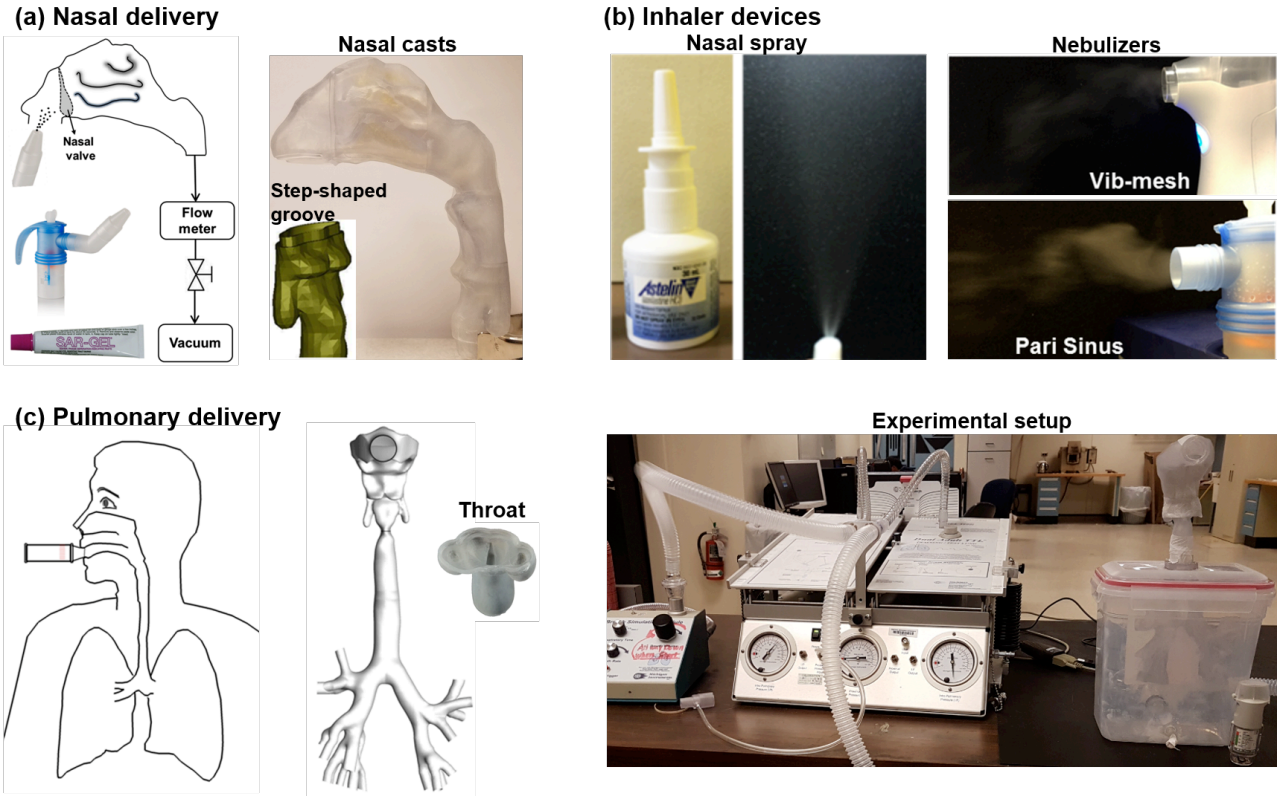

Figure 1: Experimental setup for visualization of nasal and pulmonary delivery; (**a**) diagram of nasal delivery and nasal airway casts; (**b**) inhalation devices: nasal sprays and two types of nebulizers, and (**c**) setup of pulmonary drug delivery.

Figure **1c** shows the experimental setup used for pulmonary drug delivery. The lung model was positioned in a 5-liter container that represents the typical adult lung volume [18]. A breathing machine (Michigan Instruments, Grand Rapids, MI) or a vacuum pump (Robinair, Warren, MI) was used to ventilate the container to simulate either tidal or steady respirations (Figure **1c**). Sar-Gel was coated evenly on the inside walls of the replicas [12]. Photos were taken immediately after the drug release. Each test was repeated five times. Control tests were conducted to consider the effect of the ambient air on Sar-Gel, which exhibited no perceivable changes in five minutes This insensitiveness of Sar-Gel to ambient moistures were also observed by Kundoor and Dalby [10,11].

2.2. Computational Simulations

Complimentary computational simulations were performed in pulmonary drug delivery. Computational meshes were created using ANSYS ICEM 10 (Ansys, Inc.) with body-fitted elements near the inner airway surface [19]. Grid independence study was conducted and the final computational mesh had 3.6 million elements [20]. The airflows were isothermal and incompressible, with flow regimes possible for laminar, transitional, and turbulent flows. To resolve this multi-regime flows, large eddy simulation (LES) was selected in this study due to its capacity to capture flow transitions and vortex details [21,22]. Chemical species transport model enhanced with finite particle inertia was employed to simulate the vapor transport and deposition [23,24]. Flow simulation package ANSYS Fluent (Canonsburg, PA) was used to simulate both airflow and vapor dynamics.

3. RESULTS

3.1. Nasal Delivery with Sprays and Nebulizer

Due to different exiting speeds and droplet sizes from nasal sprays and nebulizers, the deposition distributions is also very different. Figure **2** shows the nasal deposition distribution (visualized using Sar-Gel) for a typical nasal spray (Nasonex) and vibrating-mesh nebulizer [25]. The majority of the dose was filtered out by the nasal valve (Figure **2a**). Dripping was observed due to local droplet accumulation. This high filtration rate may result from the high inertia of large sprays (70-90 μm) with relatively high speeds. Considering the nebulizer in Figure **2b**, predominant doses were observed in the turbinate region while only a small portion deposited in the superior meatus. This supports the understanding that current nasal devices deliver limited dosage to the olfactory region and therefore, advanced delivery techniques are needed to improve the olfactory targeting efficiency.

The output and deposition fraction from the nasal spray was also quantified (Figure **2a**). Compared to the

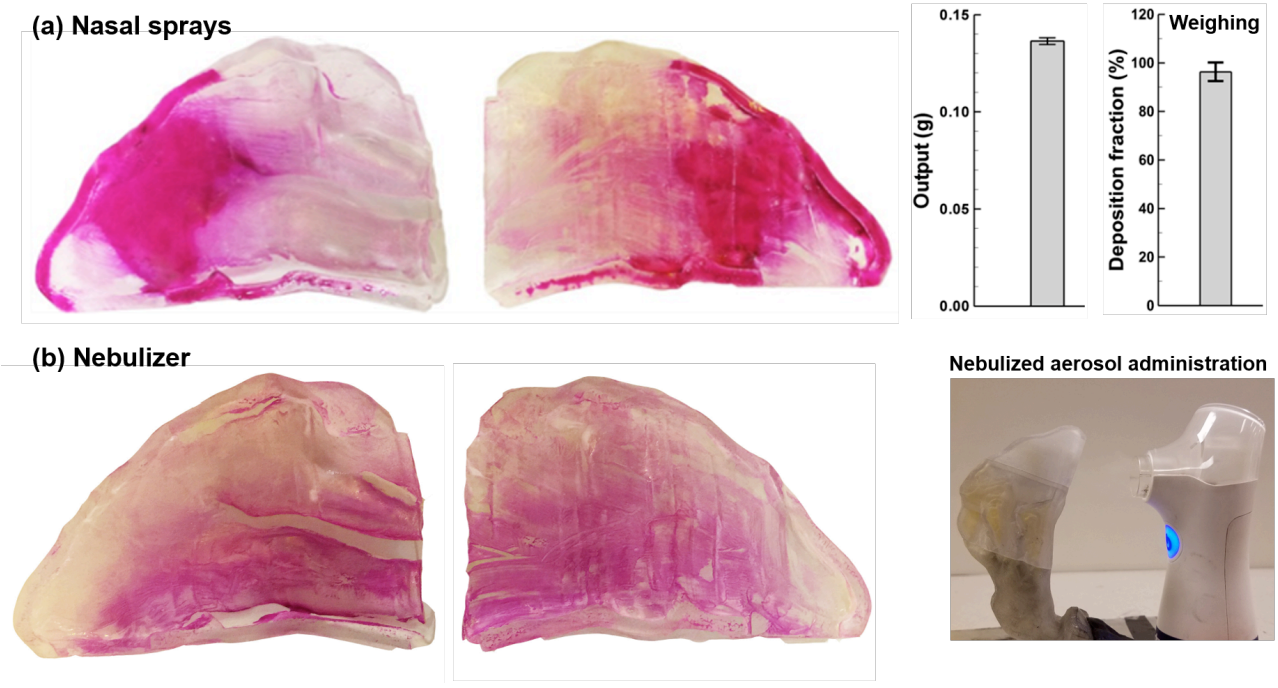

Figure 2: Nasal deposition distributions visualized using Sar-Gel; (**a**) nasal sprays with quantification of spray output and deposition and (**b**) nebulizer.

unit of *mg* for nebulizer outputs, the spray output is approximately two orders of magnitude higher. Due to the large aerosol diameters (70-90 μm), almost all droplets (96% ± 4%) will deposit in the nasal cavity. In contrast, nebulized aerosols are in the range of 1-7 μm and can lead to different deposition rates and deposition patterns due to their small inertia.

3.2. Pulmonary Drug Delivery

Comparison of deposition distributions between experimental tests and computational simulations is displayed in Figure **3**. The inhalation flow rate was 20 L/min that represented human normal breathing and the nebulizer used was vibrating mesh type. From Figure **3a**, an excellent match was obtained between the Sar-Gel generated deposition image and the computationally predicted deposition patterns, indicating that the computational modeling herein indeed captured the aerosol transport and deposition mechanisms. Particularly, there exist several positions with highly similar *in vitro*-CFD deposition patterns. First, CFD successfully predicted the crescent-shaped deposition hot spot in the sub glottal region. The two streaks in the middle front trachea also matched closely between the experimental and computational results.

To quantify the sub-regional deposition, five sections are delineated: oral cavity, throat, trachea, G1, G2-3, and G4-5, as displayed in Figure **3c**. The lumen volumes and surface areas of each region are listed in Figure **3d**. The area-to-volume ratio (A_S/Vol) denotes the complexity of the airway morphology. For instance, the area-to-volume ratio is 2.0 for G1, 2.7 for G1-2, and 4.6 for G4-5. The deposition fraction (DF) in each region is listed in the third column of Figure **3d**. There are 7.1% depositing in G1 and 7.4% in G2-3, in comparison to 25.7% in the oral cavity, 5.5% in the throat, and 9.1% in the trachea. The dose in each region per unit area was also computed and listed in the fourth column. The throat received the highest dose per unit area due to its flow-limiting nature. Downstream of the throat, the dose per area gradually decreases along the respiratory tract. This decrease results from two factors: (1) the depletion of inhaled vapor due to upstream deposition, and (2) the increased surface area and morphology from the trachea to G5.

Airflow field and vapor transport in the human upper airway for an inhalation flow rate of 20 L/min are shown in Figure **4**. Considering the midplane view of the MT and TB regions (Figure **3a**), the maximum speed is observed in the glottis, which has the minimum cross-

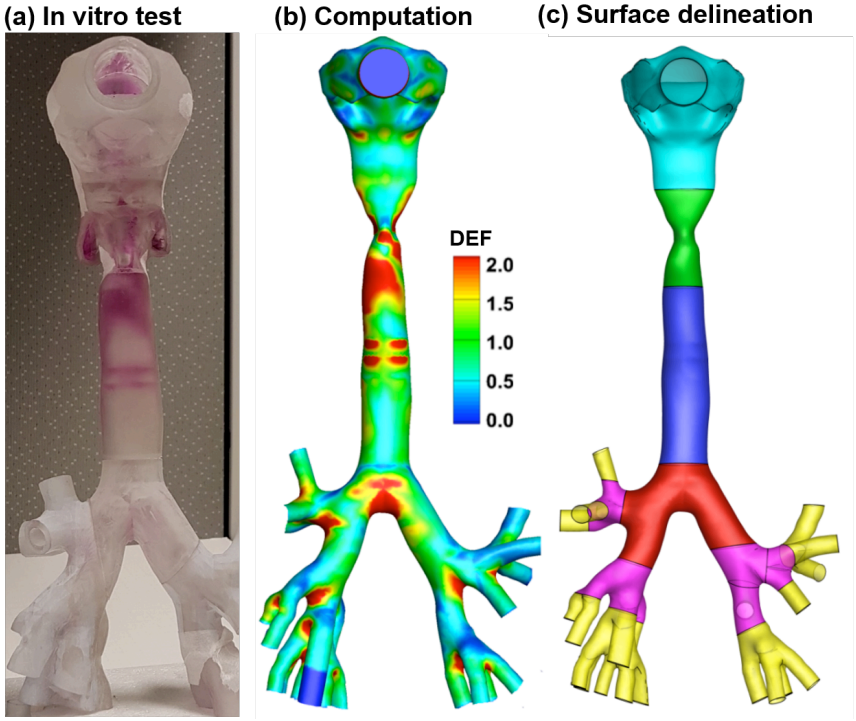

(d) Dimension and deposition

	Volume (ml):	Area (cm^2):	DF (%):	Dose per area (%/cm^2):
Oral:	60.6	130.0	25.7	0.198
Throat:	8.4	23.4	5.5	0.234
Trachea:	26.7	52.9	9.1	0.172
G1:	24.5	48.3	7.1	0.147
G2-3:	22.1	60.3	7.4	0.123
G4-5:	26.9	124.1	13.3	0.107
Total:	169.2	439.0	68.1	0.155

Figure 3: Comparison of deposition distributions in the mouth-lung geometry between experiments and computational predictions; (**a**) *in vitro* tests; (**b**) computational prediction; (**c**) surface divided into different sections, and (d) dimension and deposition of different sections.

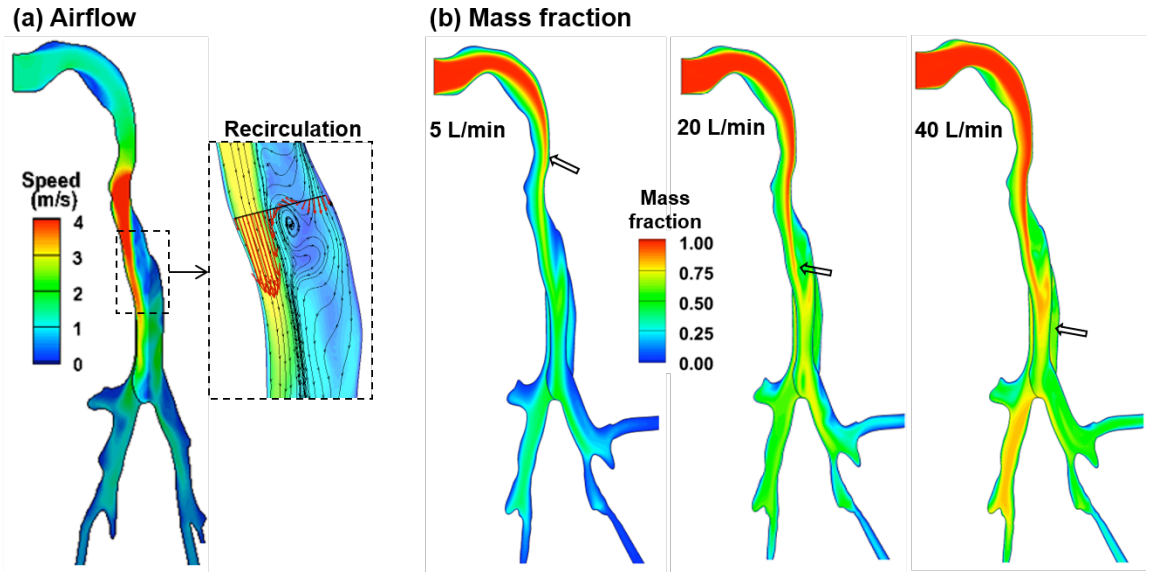

Figure 4: Airflow and vapor transport in the mouth-lung model; (**a**) airflow field and (**b**) mass fraction of the inhaled vapor species at different inhalation rates: 5 L/min, 20 L/min, 40 L/min.

sectional area and is the flow-limiting area in the human upper airway. Because of the jet effect of the laryngeal jet, recirculation zone forms in the dorsal region of the trachea (Figure **4a**). To demonstrate the effects of recirculation motion on the flow field, streamlines are plotted in the TB dorsal regions. These streamlines are highly heterogeneous because of the complex vortex patterns. Considering the vapor transport in Figure **3b**, the vapor concentration is the highest at the inlet and decreases progressively due to the wall deposition. This decrease is faster at lower inhalation flow rates because of the prolonged vapor residence time but is significantly minimized at high flow rates (say 40 L/min).

3.3. Colorimetry-Mass Correlation

Figure **5** shows the development of empirical colorimetry-mass relation. The pink color increases its intensity with increasing exposure time (Figure **5a**), which was quantified using the image processing package in Matlab, as shown in Figure **5b**. The relationship correlating the vapor mass and color intensity (colorimetry) is approximated as (Figure **5c**):

$$m = 1.790\log(x) - 0.677 \quad (1)$$

Figure **6a** shows the surface depositions inside the nose with different nebulizers (PARI Sinus and jet nebulizers) and breathing conditions (0, 10, 18 L/min).

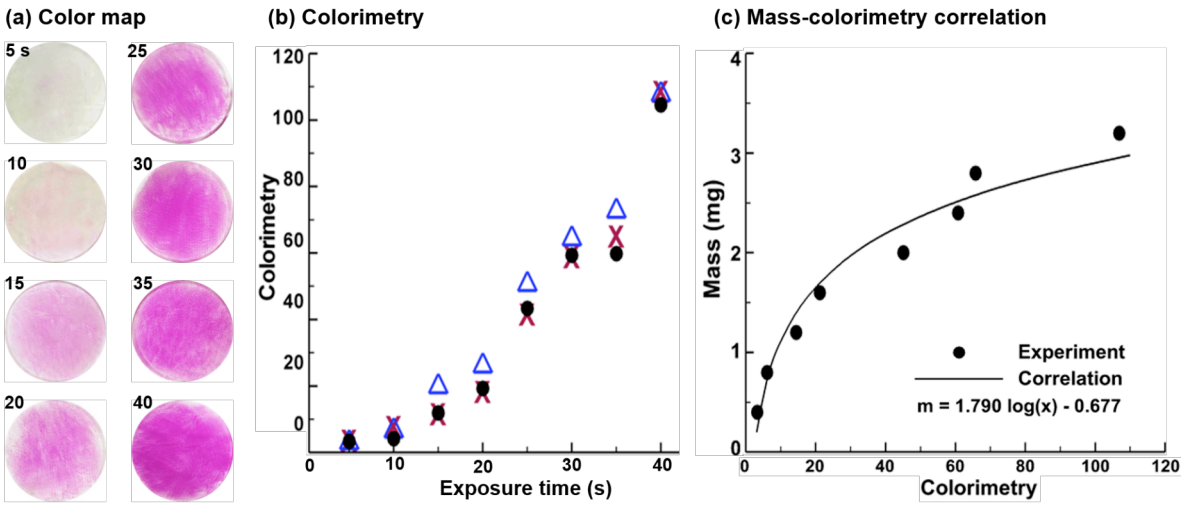

Figure 5: Quantification of Sar-Gel color variation; (**a**) color map versus exposure time; (**b**) color quantification (colorimetry), and (**c**) mass-colorimetry correlation.

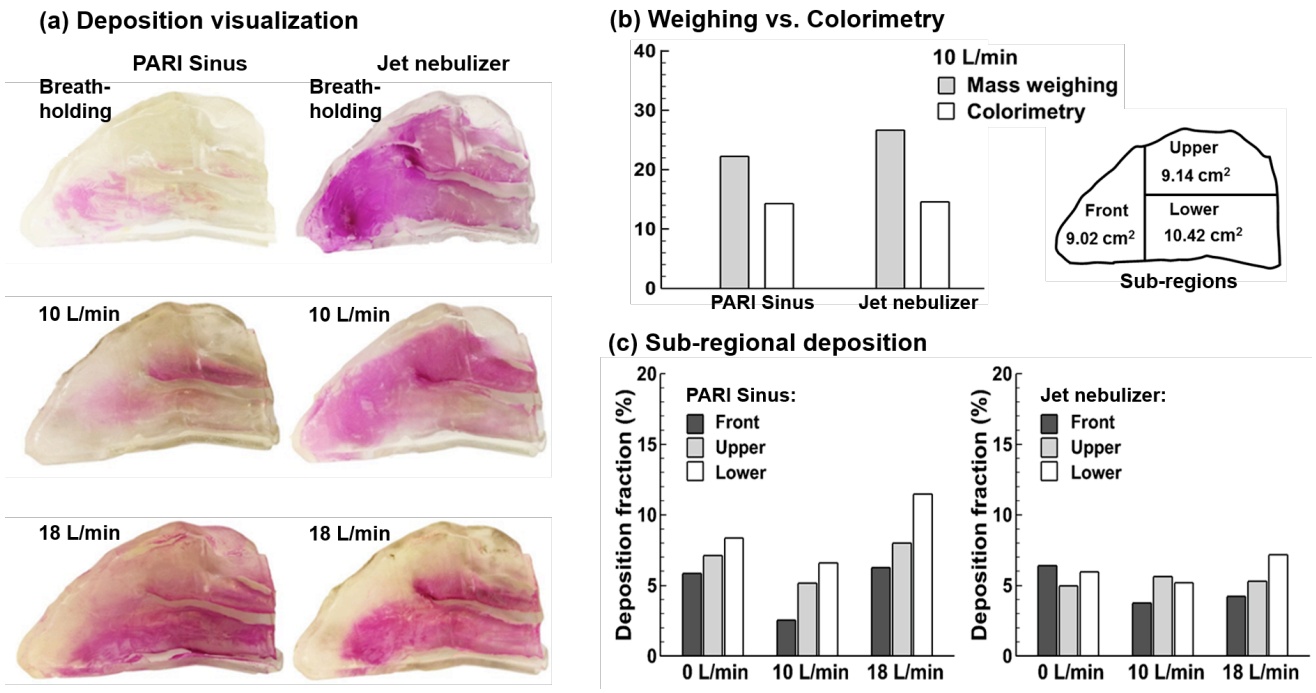

Figure 6: *In vitro* tests of nasal delivery using a PARI Sinus nebulizer and a jet (Philips) nebulizer; (**a**) surface deposition distributions in the left nasal passage at three inhalations rates (0, 10, and 18 L/min); (**b**) validation of the colorimetry methods with the direct weighing method at 10 L/min, and (**c**) sub-regional deposition fractions in the front, upper, and lower nose. The delineation of the three sub-regions is also shown.

Distinct deposition distributions were observed in Figure **6a**, ranging from scattered to dense diffusive doses on the wall. Substantial differences were observed between different breathing conditions using PARI Sinus. At 18 L/min, more vapor aerosols were filtered by the upper nose than at 10 L/min and breath-holding. Considering the jet nebulizer, deposition profiles appeared diffusive for all inhalation rates considered. Most droplets were deposited in the anterior nose at breath-holding. Deposition in the upper nose decreased at higher inhalation flow rates.

The newly developed colorimetry method was used to quantify the nasal deposition fractions using PARI Sinus and jet nebulizers, which was further validated against the deposition fractions measured by weighing the mass differences at 10 L/min (Figure **6b**). The colorimetry approach underpredicted the mass-weighing data by approximately 25-35%, but exhibited a similar trend in deposition variation, suggesting an inherent agreement between these two methods. The underprediction of the colorimetry method might result from the phenomenon that certain aerosols deposited below the turbinate and didn't show up in the Sar-Gel image.

Sub-regional deposition fractions in front, upper, lower nose were characterized using the colorimetry method (Figure **6c**). Deposition fractions in these regions respond differently to the types of nebulizer and inhalation rates. In this regard, the Sar-Gel method appears to be a simple and efficient method to test the performance of inhalation devices, or to identify the optimal combination of inhalation devices and delivery protocols for targeted drug delivery.

One such example is the technique of point drug delivery, which can effectively enhance dosages in the targeted region, while reducing drug wastes in other regions. This technique was developed based on the observation that aerosol particles released at one specific point of the nostril will consistently deposit in certain regions of the nasal passage [26]. For instance, aerosols released into the tip of the nostril will deposit in the upper nose and olfactory region, while aerosols released into the base of the nostril will most likely deposit in the lower turbinate and nasal floor. Adaptors of small diameters (1-1.5 mm) should be used to concentrate the released aerosols. Figure **7a** shows the concentrated aerosol streams from the adaptors coupled with either an ultrasound nebulizer or a vibrating mesh nebulizer. In this example, the aerosols were targeted to the middle meatus and potentially the ostiomeatal complex underneath the middle conchae. Nebulized aerosols were released into the middle of the nostril. The resultant deposition distributions are

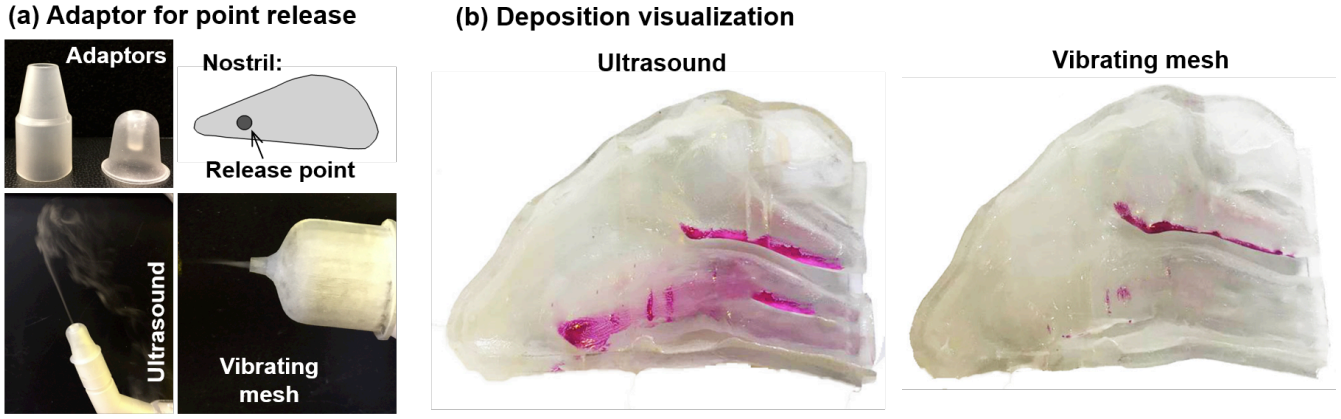

Figure 7: Point-release for targeted drug delivery; (**a**) adaptors used for drug point release, and (**b**) concentrated deposition patterns using two types of nebulizers.

displayed in Figure **7b**, which is remarkably concentrated in comparison to those without point-release. For both nebulizers, the doses accumulated at the edges of the middle conchae, as intended. However, the vibrating mesh nebulizer outperformed the ultrasound nebulizer in dispensing the does to the target only. There are also considerable deposition accumulations in the lower conchae using the ultrasound nebulizer. These accumulated drug aerosols will be eventually wasted or induce unwanted health effects.

4. DISCUSSIONS AND CONCLUSION

Highly heterogeneous deposition profiles of inhaled vapor were observed for all inhaler devices and breathing conditions considered. Excellent agreements were achieved between the Sar-Gel generated surface deposition image and the computationally predicted vapor deposition pattern in the lung casts, instilling confidence into this newly proposed visualization method. Particularly, both the experiment and simulation captured the crescent-shaped deposition hot spots downstream of the throat and the two streaks in the middle trachea (Figure **3a**). The proposed Sar-Gel approach can be readily modified to investigate drug dispensing to other regions in the respiratory tract, using different devices, and with different delivery protocols.

To reliably quantify the total and olfactory deposition rates, it is desirable to use a shell-like nasal cast as implemented in this study (Figure **1**) as opposed to the conventional block-type casts. In most previous studies, nasal airway cast replicas were developed by subtracting a block with the nasal airway to obtain the airway space within the solid block.[27,15,16] The weights of such block-type casts are typically close to or beyond the capacity of high-precision lab scales. For instance, the maximum weight capacity of the scale used in this study (Sartorius R160P, 0.01 mg precision) is 160 g. A low precision (1mg and above) scale cannot reliably measure the differential weight before and after the nebulizer administration due to the low dosages. This requirement is more pronounced when measuring the regional deposition rate, such as the olfactory dosage, which ranges 0.5-2 mg for 20-second aerosol administration. Another issue is that the measurement of such small quantities can be affected by the slightest variations in the surrounding, such as noise, vibration, breeze, magnetic field, temperature, and humidity. Care was taken in this study to minimize such influences. The measurements were conducted in a quiet room free from noise and vibration. After each experiment, the nasal casts were washed, dried in the oven to remove moistures, and left in the lab for an additional hour before the next use to let the cast surface become fully equilibrium with the environment (Figure **2**). These procedures were found to be essential to minimize the complications from the temperature and humidity when measuring vapor depositions; large fluctuations had been observed otherwise due to vapor absorption or evaporation.

Sar-Gel visualization method and numerical modeling can be complementary to each other in the optimization of inhalation protocols. The Sar-Gel shows the distribution of aerosol deposition in a direct and qualitative manner, whereas the computational simulations can provide details of the airflow and aerosol behaviors behind the observed aerosol deposition. While computational simulations are more cost-efficient, they are limited by many simplifications that inevitably reduced their physical realism to

represent the *in vivo* or experimental scenarios. To this end, the Sar-Gel method can provide more clinically relevant results and include realistic factors that are still difficult, if not prohibitive, to computational methods. Although possible to be considered in CFD, these factors require either advanced algorithms or large resources. Recent efforts have been taken to numerically include the effects of polydisperse aerosols [28], electric charges [29,17,30], hygroscopic growth [31,32], compliant geometries [33,30], more bronchiole generations [34], and inter-subject uncertainties [35].

IN SUMMARY

1. Sar-Gel visualization was demonstrated to provide a simple and reliable method to reveal and quantify deposition distributions inside airways that had been inaccessible to standard measurements.

2. Sectional airway casts with step-shaped grooves were essential to ensure airtight during *in vitro* tests.

3. Computational simulations and Sar-Gel visualization were complimentary to each other in studying nasal and pulmonary drug delivery by attending to both flow details and the resultant deposition distribution, which facilitates the discovery of underlying transport and deposition mechanisms.

4. Sar-Gel visualization method can be used as a platform to design and test new devices or delivery protocols, such as the point drug release.

CONFLICT OF INTEREST

The authors report no conflicts of interest in this work.

REFERENCES

[1] Sakai H, Watanabe Y, Sera T, Yokota H and Tanaka G. Visualization of particle deposition in human nasal cavities. Journal of Visualization 2015; 18(2): 349-357. https://doi.org/10.1007/s12650-014-0238-x

[2] Sznitman J, Sutter R, Altorfer D, Stampanoni M, Rosgen T and Schittny JC. Visualization of respiratory flows from 3D reconstructed alveolar airspaces using X-ray tomographic microscopy. Journal of Visualization 2010; 13(4): 337-345. https://doi.org/10.1007/s12650-010-0043-0

[3] Dolovich MB. Measuring total and regional lung deposition using inhaled radiotracers. Journal of Aerosol Medicine and Pulmonary Drug Delivery 2001; 14(1): S35-44. https://doi.org/10.1089/08942680150506321

[4] Darquenne C, Fleming JS, Katz I, Martin AR, Schroeter J. Bridging the gap between science and clinical efficacy: physiology, imaging, and modeling of aerosols in the lung. Journal of Aerosol Medicine and Pulmonary Drug Delivery 2016; 29(2): 107-126. https://doi.org/10.1089/jamp.2015.1270

[5] Xi J, Yuan JE, Zhang Y, Nevorski D, Wang Z and Zhou Y. Visualization and quantification of nasal and olfactory deposition in a sectional adult nasal airway cast. Pharmaceutical Research 2016; 33(6): 1527-1541. https://doi.org/10.1007/s11095-016-1896-2

[6] Inthavong K, Tian ZF, Li HF, Tu JY, Yang W, *et al*. A numerical study of spray particle deposition in a human nasal cavity. Aerosol Science and Technology 2006; 40(11): 1034-U1033. https://doi.org/10.1080/02786820600924978

[7] Zhang Z and Martonen TB. Deposition of ultrafine aerosols in human tracheobronchial airways. Inhalation Toxicology 1997; 9: 99-110. https://doi.org/10.1080/089583797198295

[8] Inthavong K, Tao Y, Petersen P, Mohanarangam K, Yang W and Tu J. A smoke visualization technique for wake flow from a moving human manikin. Journal of Visualization 2016; 19: 1-13.

[9] Guo Y, Laube B and Dalby R. The effect of formulation variables and breathing patterns on the site of nasal deposition in an anatomically correct model. Pharmaceutical Research 2005; 22(11): 1871-1878. https://doi.org/10.1007/s11095-005-7391-9

[10] Kundoor V and Dalby RN. Assessment of nasal spray deposition pattern in a silicone human nose model using a color-based method. Pharmaceutical Research 2010; 27(1): 30-36. https://doi.org/10.1007/s11095-009-0002-4

[11] Kundoor V and Dalby RN. Effect of formulation- and administration-related variables on deposition pattern of nasal spray pumps evaluated using a nasal cast. Pharmaceutical Research 2011; 28(8): 1895-1904. https://doi.org/10.1007/s11095-011-0417-6

[12] Xi J, Wang Z, Nevorski D, White T and Zhou Y. Nasal and olfactory deposition with normal and bidirectional intranasal delivery techniques: *in vitro* tests and numerical simulations. Journal of Aerosol Medicine and Pulmonary Drug Delivery 2017; 30(2): 118-131. https://doi.org/10.1089/jamp.2016.1295

[13] Xi J, Yang T, Talaat K, Wen T, Zhang Y, *et al*. Visualization of local deposition of nebulized aerosols in a human upper respiratory tract model. Journal of Visualization, In press 2017; 1-13. https://doi.org/10.1007/s12650-017-0456-0

[14] Xi J, Berlinski A, Zhou Y, Greenberg B and Ou X. Breathing resistance and ultrafine particle deposition in nasal-laryngeal airways of a newborn, an infant, a child, and an adult. Annals of Biomedical Engineering 2012; 40(12): 2579-2595. https://doi.org/10.1007/s10439-012-0603-7

[15] Zhou Y, Guo M, Xi J, Irshad H and Cheng YS. Nasal deposition in infants and children. Journal of Aerosol Medicine and Pulmonary Drug Delivery 2014; 27(2): 110-116. https://doi.org/10.1089/jamp.2013.1039

[16] Zhou Y, Xi J, Simpson J, Irshad H and Cheng YS. Aerosol deposition in a nasopharyngolaryngeal replica of a 5-year-old child. Aerosol Science and Technology 2013; 47(3): 275-282. https://doi.org/10.1080/02786826.2012.749341

[17] Xi J, Si X and Longest W. Electrostatic charge effects on pharmaceutical aerosol deposition in human Nasal–Laryngeal airways. Pharmaceutics 2014; 6(1): 26-35. https://doi.org/10.3390/pharmaceutics6010026

[18] Jones RL and Nzekwu MMU. The effects of body mass index on lung volumes. Chest 2006; 130(3): 827-833. https://doi.org/10.1378/chest.130.3.827

[19] Si XA and Xi J. Modeling and simulations of olfactory drug delivery with passive and active controls of nasally inhaled pharmaceutical aerosols. Journal of Visualized Experiments 2016; 111: e53902. https://doi.org/10.3791/53902

[20] Xi J, Kim J, Si XA and Zhou Y. Diagnosing obstructive respiratory diseases using exhaled aerosol fingerprints: A feasibility study. Journal of Aerosol Science 2013; 64: 24-36. https://doi.org/10.1016/j.jaerosci.2013.06.003

[21] Si X, Xi J and Kim J. Effect of laryngopharyngeal anatomy on expiratory airflow and submicrometer particle deposition in human extrathoracic airways. Open Journal of Fluid Dynamics 2013; 3(4): 286-301. https://doi.org/10.4236/ojfd.2013.34036

[22] Xi J, Si X, Kim J, Su G and Dong H. Modeling the pharyngeal anatomical effects on breathing resistance and aerodynamically generated sound. Medical and Biological Engineering and Computing 2014; 52(7): 567-577. https://doi.org/10.1007/s11517-014-1160-z

[23] Dhand R. Nebulizers that use a vibrating mesh or plate with multiple apertures to generate aerosol. Respiratory Care 2002; 47(12): 1406-1416.

[24] Waldrep JC and Dhand R. Advanced nebulizer designs employing vibrating mesh/aperture plate technologies for aerosol generation. Current Drug Delivery 2008; 5(2): 114-119. https://doi.org/10.2174/156720108783954815

[25] Xi J, Si XA, Kim J, Zhang Y, Jacob RE, Kabilan S and Corley RA. Anatomical details of the rabbit nasal passages and their implications in breathing, air conditioning, and olfaction. The Anatomical Record 2016; 299: 853-868. https://doi.org/10.1002/ar.23367

[26] Si X, Xi J, Kim J, Zhou Y and Zhong H. Modeling of release position and ventilation effects on olfactory aerosol drug delivery. Respiratory Physiology & Neurobiology 2013; 186(1): 22-32. https://doi.org/10.1016/j.resp.2012.12.005

[27] El Taoum KK, Xi J, Kim JW and Berlinski A. *In vitro* Evaluation of Aerosols Delivered *via* the Nasal Route. Respir Care 2015; 60: 1015-1025. https://doi.org/10.4187/respcare.03606

[28] Xi J, Yuan JE and Si XA. Simulation study of electric-guided delivery of 0.4 μm monodisperse and polydisperse aerosols to the ostiomeatal complex. Computers in Biology and Medicine 2016; 72: 1-12. https://doi.org/10.1016/j.compbiomed.2016.03.001

[29] Xi J, Si X and Gaide R. Electrophoretic particle guidance significantly enhances olfactory drug delivery: a feasibility study. Plos One 2014; 9(1): e86593. https://doi.org/10.1371/journal.pone.0086593

[30] Xi J, Yuan J, Alshaiba M, Cheng D, Firlit Z,*et al*. Design and testing of electric-guided delivery of charged carticles to the olfactory region: experimental and numerical studies. Current Drug Delivery 2016; 13(2): 265-274. https://doi.org/10.2174/1567201812666150909093050

[31] Kim J, Xi J and Si XA. Dynamic growth and deposition of hygroscopic aerosols in the nasal airway of a 5-year-old child. International Journal for Numerical Methods in Biomedical Engineering 2013; 29(1): 17-39. https://doi.org/10.1002/cnm.2490

[32] Zhang Z, Kleinstreuer C and Kim CS. Water vapor transport and its effects on the deposition of hygroscopic droplets in a human upper airway model. Aerosol Science and Technology 2006; 40: 52-67. https://doi.org/10.1080/02786820500461154

[33] Talaat K and Xi J. Computational modeling of aerosol transport, dispersion, and deposition in rhythmically expanding and contracting terminal alveoli. Journal of Aerosol Science 2017; 112: 19-33. https://doi.org/10.1016/j.jaerosci.2017.07.004

[34] Xi J, Zhao W, Yuan JE, Cao B and Zhao L. Multi-resolution classification of exhaled aerosol images to detect obstructive lung diseases in small airways. Computers in Biology and Medicine 2017. https://doi.org/10.1016/j.compbiomed.2017.05.019

[35] Lu J, Xi J and Langenderfer JE. Sensitivity analysis and uncertainty quantification in pulmonary drug delivery of orally inhaled pharmaceuticals. Journal of Pharmaceutical Sciences 2017; 106(11): 3303-3315. https://doi.org/10.1016/j.xphs.2017.06.011

Received on 23-12-2017 Accepted on 29-12-2017 Published on 31-12-2017

DOI: http://dx.doi.org/10.20941/2310-9394.2017.05.1